MXene Aerogel for Efficient Photothermally-Driven Membrane Distillation with Dual-Mode Antimicrobial Capability

1   **MXene Aerogel for Efficient Photothermally-Driven Membrane Distillation**

2   **with Dual-Mode Antimicrobial Capability**

3   Sisi Cao,[1,†] Xuanhao Wu,[2,†] Yaguang Zhu,[2] Prashant Gupta,[1] Adrian Martinez,[2] Yunzhu Zhang,[2]

4   Deoukchen Ghim,[2] Yixuan Wang,[1] Lin Liu,[1] Young-Shin Jun[2]* Srikanth Singamaneni[1]*

5

6   *[1]Department of Mechanical Engineering and Materials Science, Institute of Materials Science*

7   *and Engineering, Washington University in St. Louis, St Louis, MO, 63130, USA*

8   *[2]Department of Energy, Environmental and Chemical Engineering, Washington University in St.*

9   *Louis, St. Louis, MO, 63130, USA*

     †These authors contributed equally

10   *To whom correspondence should be addressed: singamaneni@wustl.edu (SS) and

11   ysjun@wustl.edu (YJ).

12   **Abstract**

13   Solar-driven desalination, which involves the conversion of solar energy to heat for freshwater

14   generation, has been recognized as an attractive and sustainable desalination technology to

15   alleviate freshwater shortage. In particular, photothermally-driven membrane distillation (PMD) is

16   a highly promising solar-driven desalination technology, especially in remote regions and disaster-

17   struck communities, where no power infrastructure or waste heat from industrial plants is available.

18   MXene, more specifically $Ti_3C_2T_x$, with excellent photothermal properties, easy processability, and

19   electrical conductivity offers a great opportunity for realizing highly efficient, stable and

20   multifunctional PMD membranes. Herein, we realize a MXene composite aerogel comprised of

21   hydroxyapatite nanowires and poly(vinyl alcohol) with high thermal efficiency (61%) and water

22   flux (0.72 $kg \cdot m^{-2} \cdot h^{-1}$) under 0.8 sun irradiation (0.8 $kW \cdot m^{-2}$), representing the first validation of

23   highly efficient MXene-based PMD systems in treating ambient saline water. Owing to the strong

24   interfacial interaction (*i.e.*, hydrogen bonding) between the building blocks, the MXene composite

25   aerogel with high porosity (up to 91%) exhibited excellent mechanical stability. This highly

26   interconnected porous network offers low resistance to vapor transport and low thermal

27   conductivity, which minimizes conductive heat transfer across the aerogel, thus maximizing the

28   thermal efficiency. Furthermore, the outstanding bactericidal activity induced by solar irradiation

29   or electric potential makes the MXene composite aerogel a highly attractive candidate for PMD in

30   the real world.

31   **Keywords:** MXene, desalination, membrane distillation, photothermal, antibiofouling

1. Introduction

To overcome the limited freshwater availability, increasing water demand and pollution caused by human activity, various desalination technologies have been developed to relieve the water scarcity, including reverse osmosis and thermal distillation.[1,2] However, they still have challenges to address freshwater shortage because of high energy consumption and high carbon footprint, especially for developing countries or rural areas where large power plants are not available.[3] To minimize the non-renewable energy consumption and reduce the possible adversary impacts on the environment during freshwater generation, emerging technologies, such as solar steam generation, are highly promising.[4-6] For solar stream generation, the advances in materials and the design of interfacial evaporators have prompted the thermal efficiency up to 90%, but the difficulty associated with freshwater collection from the generated vapor has still hindered their application in the real world.[7] For instance, the reported thermal efficiency decreases by 60–70% after integrating a solar steam generator with water collection system.[8,9] To address this challenge, another solar-driven desalination technology, photothermally-driven membrane distillation (PMD), has been proposed, which integrates membrane distillation with photothermal membrane.[10-13] Upon solar irradiation, the surface heating is achieved on the photothermal membrane, and the vapor is generated at the interface between the feed water and the hydrophobic photothermal membrane. Driven by the vapor pressure caused by the temperature difference across the photothermal membrane, the vapor transports from the hot feed side to the cold permeate side of the photothermal membrane, where the vapor condenses for freshwater generation.

As a new series of 2D materials, the MXene family is composed of early transition metal carbides and/or carbonitrides, with a general formula of $M_{n+1}X_n$, where M represents transition metal (e. g., Sc, Ti, Zr, Hf, V, Nb, Ta, Cr and Mo) and X is carbon and/or nitrogen.[14] Synthesized by wet-chemical etching using hydrofluoric (HF) acid or HF-containing or HF-forming etchants, the functional groups (e.g., -OH, -O and -F) are introduced on the surface of MXene,[15] and as-synthesized MXene is represented by $M_n+1X_nT_x$, where T_x refers terminal functional groups.[16] Recently, MXene has been utilized in solar-driven desalination.[17] MXene exhibits broadband light absorption and an outstanding (100%) internal light-to-heat conversion efficiency, enabling excellent photothermal performance.[18] For instance, a MXene aerogel exhibited up to 96% light absorption.[19] Another attractive property of MXene is the high hydrophilicity due to the presence of hydroxyl groups, which precludes the need to use organic solvents during the membrane fabrication.[20] In addition, the abundant hydroxyl groups favor the interaction with other materials via hydrogen bonding to achieve desired structure and enhanced mechanical properties.[21-24]

65   Owing to these appealing properties, MXene has been processed into various forms, such as

66   compact/porous film,[18, 25-27] microspheres[28] and 3D aerogels,[21, 29, 30] and has been integrated with

67   different materials to achieve high-performance solar evaporation.[25, 31] Wang and co-workers

68   have reported a compact MXene film integrated with a thermal insulator exhibited a thermal

69   efficiency of 84% under 1 kW•m^{-2} (1 sun).[18] MXene aerogel with tunable pore shape and size has

70   been demonstrated for efficient solar evaporation with thermal efficiency of 87% under 1 sun.[19]

71   Although MXene-based solar evaporators exhibit high evaporation efficiency, freshwater

72   generation efficiency significantly drops after integrating water collector. Thus, utilizing MXene in

73   PMD membranes would unlock the full capability of MXene for more efficient resource use and

74   effective clean water generation.

75   Chew and co-workers provided the first proof-of-concept of MXene in PMD and

76   demonstrated that the flux of MXene-coated polyvinylidene fluoride (PVDF) membrane was 10%

77   higher under solar irradiation than that in the absence of solar light, when treating preheated

78   saline water (65°C).[32] However, MXene-coated PVDF membrane exhibited lower flux compared

79   to pristine PVDF membrane even under 5.8 sun light illumination. Such compromised

80   performance in the presence of MXene results from the compact stacking structures of MXene,

81   which greatly increases vapor transfer resistance. In addition, the compact MXene film possesses

82   high thermal conductivity,[33, 34] which leads to large conductive heat loss across the membrane

83   during membrane distillation, consequently lowing its thermal efficiency. These issues highlight

84   the need for optimizing the MXene architecture for an enhanced membrane distillation

85   performance. The PMD performance of MXene in treating saline water at ambient temperature

86   (*i.e.*, non-preheated) has not been investigated yet. The ability to implement PMD using non-

87   preheated saline water is critical in remote regions and disaster-struck communities, where hot

88   feed water is not readily available.[35] Yet another consideration in the utilization of MXene as a

89   photothermal material is that MXene can be easily oxidized in the presence of water and oxygen.[36]

90   Most of the previous reports indicate that MXene-based photothermal membranes can achieve

91   stable evaporation performance, [37-39] but a recent report indicates the partial oxidation of MXene

92   after solar steam generation.[30] Considering that the oxidation of MXene can lead disintegration of

93   the structures and deterioration of its photothermal performance, chemical stability of MXene

94   membranes is highly important for its long-term stable desalination performance.

95   Accounting for more than 45% of all membrane fouling, biofouling is responsible for a

96   significant decline in water flux in various membrane distillation processes.[40-42] The addition of

97   disinfectants and biocides has been suggested to overcome biofouling, but some of these

98   chemical agents are toxic and induce negative effects on the environment. Physical cleaning,

99   such as ultrasonication cleaning and back flushing, increases operational costs and may cause

100   damage to the membrane. Recently, photothermal effect and electric field have been proven as

101   efficient and environment friendly methods to kill bacteria.[40, 43-47] The photothermal membrane can

102   kill bacteria effectively under sunlight irradiation owing to the photothermal effect, but it is not ideal

103   when solar light is weak. As an alternative disinfection method, the electric-field potential-driven

104   disinfection can be achieved on the membrane possessing electric conductivity. Therefore, the

105   membrane with excellent photothermal effect and electric conductivity is highly appealing to

106   achieve versatile bactericide capability.

107   Herein, we introduce a highly efficient and chemically stable MXene composite aerogel

108   for PMD with dual-mode anti-biofouling capability. In the MXene composite aerogel, polyvinyl

109   alcohol (PVA) is used as a binder material to improve the structural stability, and hydroxyapatite

110   (HA) nanowires are added to lower the thermal conductivity of the aerogel, which in turn reduces

111   the conductive heat loss.[35, 48, 49] MXene composite aerogel, fabricated using ice-template assisted

112   self-assembly, exhibits highly interconnected porous network, allowing low resistance for vapor

113   transfer. The high porosity (up to 91%) and low thermal conductivity (0.12 $W\cdot m^{-1}\cdot K^{-1}$) of the

114   composite aerogel enable high thermal efficiency, up to 61%, in treating ambient temperature

115   saline feedwater under 0.8 sun illumination (0.8 $kW\cdot m^{-2}$). We also demonstrate the outstanding

116   bactericidal activity of the MXene composite aerogel both under solar irradiation and under

117   external electric potential, thus obviating the need for harsh chemical/physical treatments for

118   bacterial lysis. This work sheds light on a great potential of MXene in realizing a highly efficient,

119   stable and biofouling-resistant photothermal membrane for high-performance PMD systems.

120   **2. Results and Discussion**

121   **2.1 Fabrication and characterization of MXene/PVA/HA aerogel**

122   MXene composite aerogel was fabricated by integrating MXene flakes with PVA and HA

123   nanowires (Figure 1). $Ti_3C_2T_x$ MXene flakes were synthesized by selectively etching the Al layer

124   from Ti_3AlC_2 precursor using HCl/LiF and followed by sonication to delaminate the multilayer

125   $Ti_3C_2T_x$ MXene. The MXene flakes can be stably suspended in water, and the solution appeared

126   dark-green in color (Figure 1). Scanning electron microscope (SEM) image revealed well-

127   exfoliated $Ti_3C_2T_x$ sheets (Figure 2A), and the thickness measured by atomic force microscope

128   (AFM) was 2.7 nm (Figure 2B). The successful preparation of $Ti_3C_2T_x$ was also confirmed by X-

129   ray diffraction (XRD) analysis, showing the shift of the (002) peak to a lower 2θ angle, from the

130   9.5° in Ti_3AlC_2 to 7.1° in $Ti_3C_2T_x$, which corresponded to *d-spacing* shift from 9.2 Å to 12.4 Å

131   (Figure 2C).[16, 50] The larger *d-spacing* in $Ti_3C_2T_x$ is ascribed to the introduction of terminal

132   functional groups (*e.g.* -OH, -O and -F) and incorporation of water molecules.[51] To fabricate

133   MXene composite aerogel, the Ti_3C_2Tx colloids, PVA solution and HA nanowires suspension were

134   mixed. PVA is added as a binder material, and the addition of PVA is important. In the absence

135   of PVA, the pristine MXene aerogel is too fragile to be peeled from the mold after freezing drying.

136   HA nanowires with outstanding flexibility were synthesized (Figure S1), by the previously report

137   using calcium oleate precursor *via* a hydrothermal method.[35] PVA and HA nanowires

138   spontaneously absorb on the MXene flakes owing to the abundant hydroxyl groups on each of

139   these components, which facilitates by hydrogen bonding. The PVA/HA-wrapped MXene flakes

140   were assembled into a 3D porous aerogel structure by freezing-induced ice crystal templating (-

141   20 °C) and subsequent freeze drying (Figure 1).
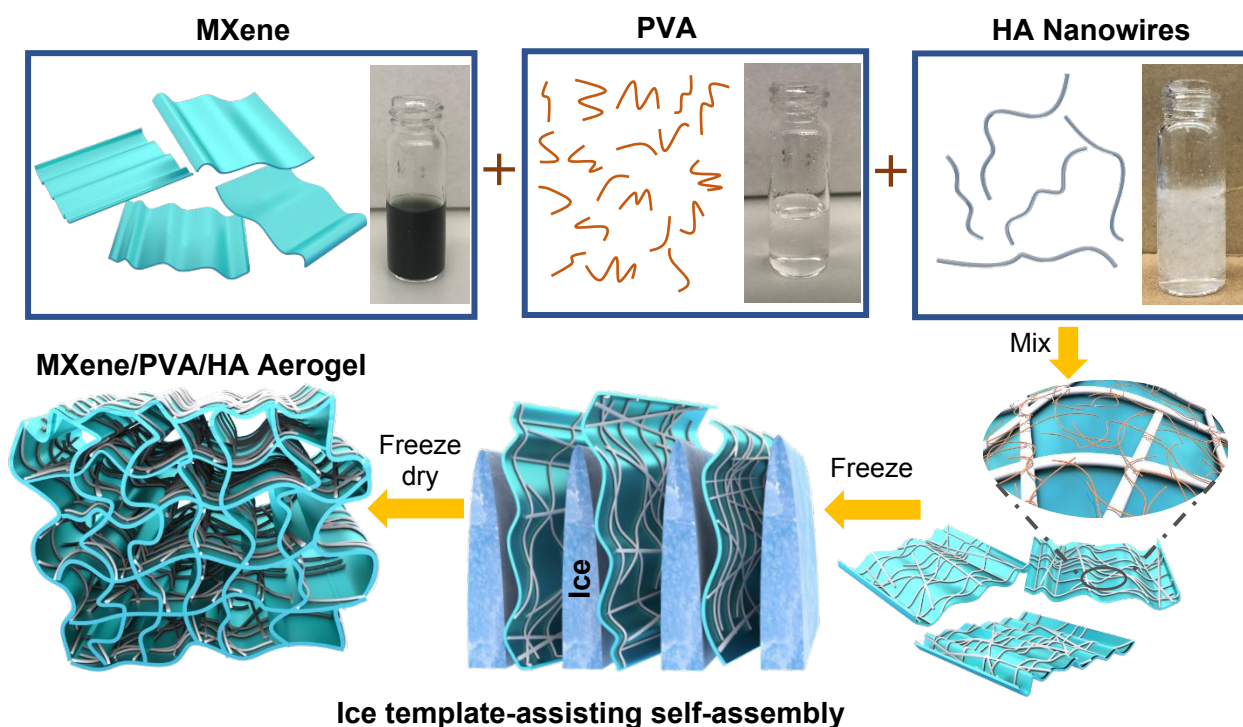
Figure 1. Schematic illustration showing the fabrication of MXene/PVA/HA aerogel using ice template-mediated self-assembly method. Upon mixing with MXene flakes, PVA and HA nanowires spontaneously wrap around the surface of MXene flakes. After freezing drying, the highly porous MXene composite aerogel is obtained.

142

143   The as-prepared black MXene/PVA/HA aerogel with a thickness of 400 µm (Figure 2H)

144   exhibited superior mechanical flexibility (Figure 2D, 2G). SEM images (Figure 2E, 2H, 2I) revealed

145   a 3D interconnected microporous structure, and the porosity was measured to be 91%. Such high

146   porosity offers low resistance for water transport during PMD and contributes to high thermal

147   efficiency. Another important factor determining the thermal efficiency of a PMD membrane is its

148   thermal conductivity. High thermal conductivity results in conductive heat transfer across the

149   membrane and reduces the temperature difference across the photothermal membrane, leading

150   to high resistance for vapor transport and thus low thermal efficiency. The $Ti_3C_2T_x$ has been

151   reported to exhibit relatively high thermal conductivity of 55.2 ± 1.7 W•m^{-1}•K^{-1}.[33] After incorporating

152   HA nanowires with low thermal conductivity and realizing stable aerogel structure with high

153   porosity, the resultant composite aerogel exhibited low thermal conductivity, 0.12 W•m^{-1}•K^{-1}

154   (Figure 3A, 3B). This low thermal conductivity enables efficient thermal insulation and high

155   temperature difference across the aerogel during PMD, leading to high driving force for vapor

156   transport.[52]
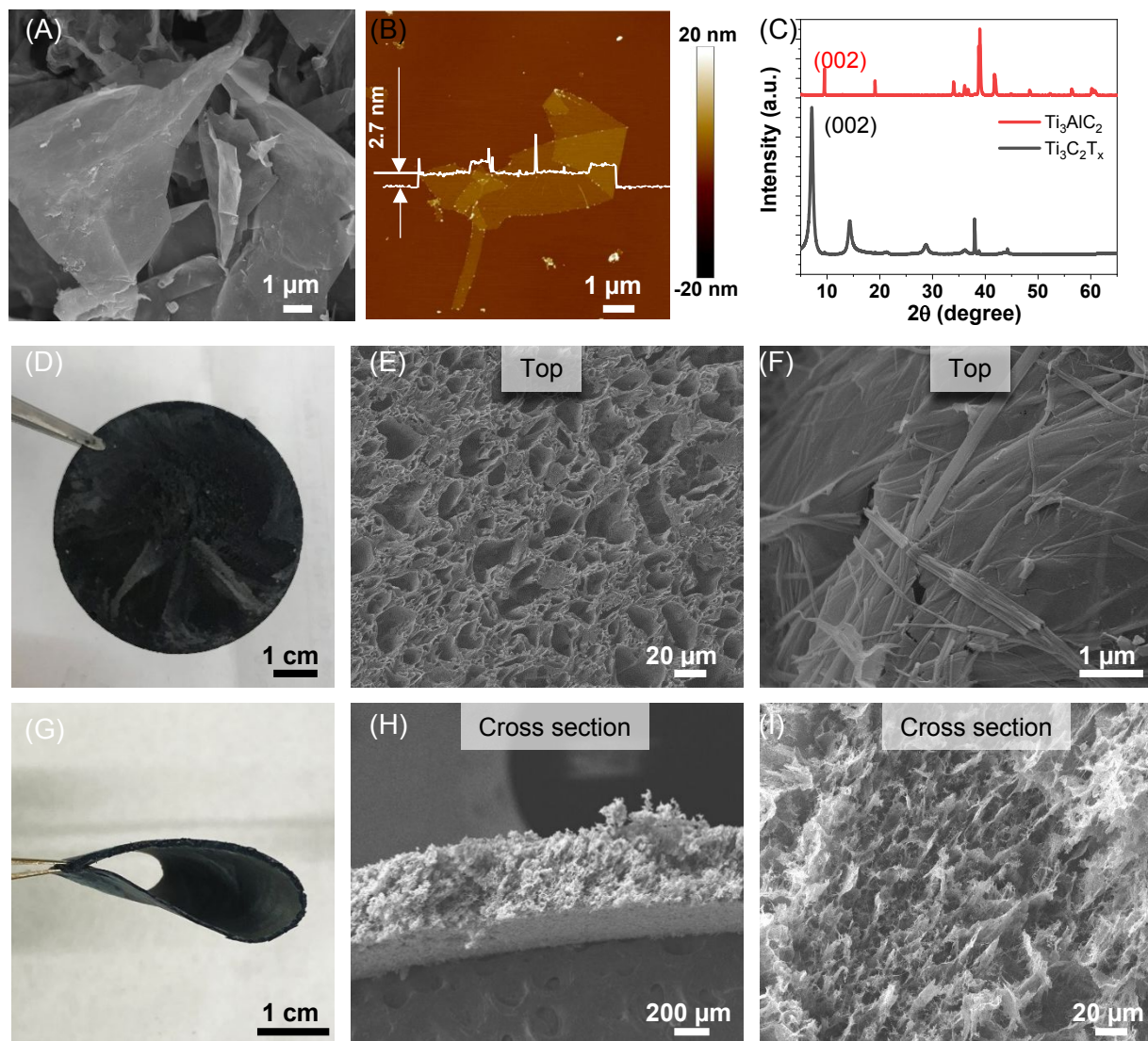
Figure 2. (A) SEM and (B) AFM image of MXene flakes. (C) Comparison of XRD patterns of Ti$_3$AlC$_2$ and Ti$_3$C$_2$Tx. Photograph of (D) as-prepared MXene/PVA/HA aerogel and (G) the deformed MXene composite aerogel. SEM images of the top surface of MXene composite aerogel in (E) low magnification and (F) high magnification. Cross-section SEM images of MXene composite aerogel in (H) low magnification and (I) high magnification.

157

158   To realize efficient desalination during PMD, the photothermal membrane needs to be

159   hydrophobic in order to prevent liquid phase transport and to ensure that only vapor can diffuse

160   across the membrane. Owing to the abundant hydroxyl groups, the composite aerogel was

161   completely hydrophilic with a water contact angle of 0°. After silanization using tridecafluoro-

162   1,1,2,2-tetrahydrooctyl)-trichlorosilane (FTCS), the contact angle of MXene/PVA/HA aerogel

163   increased to 138° (Figure 3C), indicating the successful surface hydrophobic functionalization.

164   The SEM images indicated that the highly porous network remained after this hydrophobic
165   modification (Figure S2A, S2B).
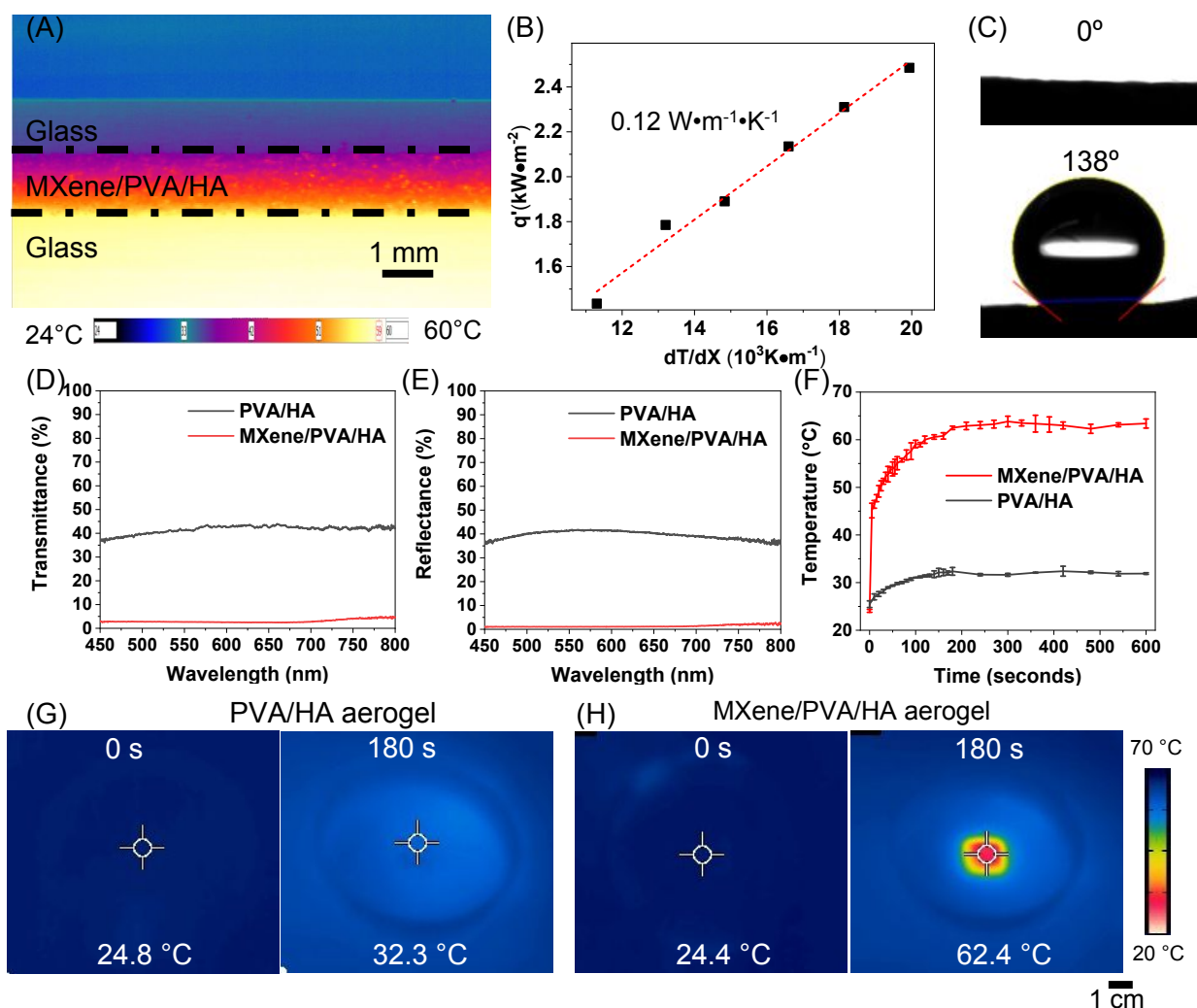
Figure 3. (A) Infrared image showing the temperature gradient along the thickness of the composite aerogel. (B) Thermal conductivity of MXene/PVA/HA aerogel. (C) Photograph showing the contact angle of MXene/PVA/HA aerogel (top) and FTCS-MXene/PVA/HA aerogel (bottom). (D) Reflectance and (E) transmittance spectra of the PVA/HA aerogel and MXene/PVA/HA aerogel. (F) Plots showing the surface temperature of the PVA/HA aerogel and MXene/PVA/HA aerogel under simulated sunlight irradiation with a power density of 0.8 kW•m^{-2} as a function of irradiation time. Infrared images showing the surface temperature of (G) the PVA/HA aerogel and (H) MXene/PVA/HA aerogel under simulated sunlight illumination with a power density of 0.8 kW•m^{-2} in open air after 180 seconds.

166

2.2 Optical and photothermal properties

168   Considering that the light absorption is critical for efficient photothermal performance, we
169   investigated the light transmittance and reflectance of composite aerogel (Figure 3D, 3E).

170   PVA/HA aerogel (without MXene) exhibited high transmittance (~42%) and reflectance (~39%) in

171   the visible region, implying relatively small light extinction (~19%). On the other hand, the

172   MXene/PVA/HA showed extremely low light transmittance (~2%) and reflectance (~1%),

173   indicating a large light extinction (~97%). The large difference in the optical properties between

174   PVA/HA aerogel and MXene aerogel stems from the broadband light absorption of MXene.[25] In

175   addition, the highly porous structure of the aerogel can result in the multiple reflection when light

176   travels through these pores and allows efficient light absorption.[31, 53] Without porous structure, a

177   compact MXene film exhibited much higher light reflectance (~8%) (Figure S3A, S3B).

178   Next, we examined the photothermal performance of MXene/PVA/HA aerogel and

179   compared it with that of PVA/HA aerogel. Current PMD systems employ 0.7~1 sun irradiation

180   to simulate the daily sunlight irradiation,[43, 54-67] so we test the photothermal performance of

181   aerogels under 0.8 sun. The surface temperature of these two aerogels in open air was monitored

182   using an infrared camera, under simulated solar light illumination at a power density of 0.8 sun

183   (Figure 3F). After light irradiation for 180 seconds, the surface temperature of the PVA/HA aerogel

184   increased from ~25 °C to ~32 °C (Figure 3G), whereas the temperature of MXene/PVA/HA

185   aerogel increased to ~62 °C under identical irradiation condition (Figure 3H). The higher surface

186   temperature realized on the MXene/PVA/HA aerogel, compared to PVA/HA aerogel, highlights

187   the outstanding light absorption and light-to-heat conversion enabled by MXene and its great

188   potential in highly efficient PMD.

189   **2.3 Photothermally-driven membrane distillation**

190   The PMD performance of MXene/PVA/HA was tested using air gap membrane distillation (AMD)

191   module (Figure S4A, S4B). The feed water was maintained to be the same as our reported test

192   conditions, 0.5 M NaCl solution at ambient temperature (20°C).[35, 68, 69] The feed water retention

193   time can affect the PMD efficiency because of its effect on the heat transfer and temperature

194   polarization on the photothermal membrane.[12, 68] Hence, different water retention times were

195   tested (2 minutes, 3 minutes, and 5 minutes). After transporting through the photothermal

196   membrane and air gap, the generated vapor finally condenses on a cold aluminum foil surface

197   (Figure 4A). The collected freshwater is quantified by measuring the weight increase of the

198   distillate as a function of irradiation time (Figure 4B). To evaluate the stability of PMD performance,

199   the MXene composite aerogel was tested for over 5 cycles (each cycle for 1 hour). Under 0.8 sun

200   illumination, the average water flux of the MXene/PVA/HA aerogel was 0.56 kg•m^{-2}•h^{-1}, 0.63

201   kg•m^{-2}•h^{-1} and 0.72 kg•m^{-2}•h^{-1} with water retention time of 2 minutes, 3 minutes, and 5 minutes,

202   respectively (Figure 4C), and the variation in the flux within the same water retention time was

203   less than 2%. The corresponding thermal efficiency of the MXene composite aerogel was
204   calculated to be 48%, 54% and 61% for feed water retention time with 2 minutes, 3 minutes and
205   5 minutes, respectively (Figure 4D).

206   The longer water retention time resulted in higher water flux and thermal efficiency. Under
207   the same incident light, the longer retention time of feed water reduces the heat loss from the
208   photothermal membrane to feed flow for more vapor generation,[12] and a larger temperature
209   difference can also be achieved across the membrane for faster vapor transfer. The longer water
210   retention time of feed water is also tested using static feed water. During 1-hour test, the water
211   flux was 0.84 kg•m^{-2}•h^{-1}, corresponding to thermal efficiency of 72%. However, after uninterrupted
212   3-hour and 6-hour operation, the water flux reduced to 0.76 kg•m^{-2}•h^{-1} and 0.66 kg•m^{-2}•h^{-1}
213   respectively. In the static feed water system, the salt concentration gradually increases with longer
214   operation time, and high salt concentration of feed water leads to a decline in the water flux.[70] In
215   addition, increasing the water retention time can also lead to a decline in water flux as the slow
216   feed rate increases the salt fouling propensity, eventually blocking vapor transport channels.[2, 71]
217   Within the tested range of water retention time, high water flux can be obtained without salt
218   accumulation on the composite aerogel when the water retention time of feed water is 5 minutes.
219   However, further investigation needs to be conducted to determine optimal water retention time.
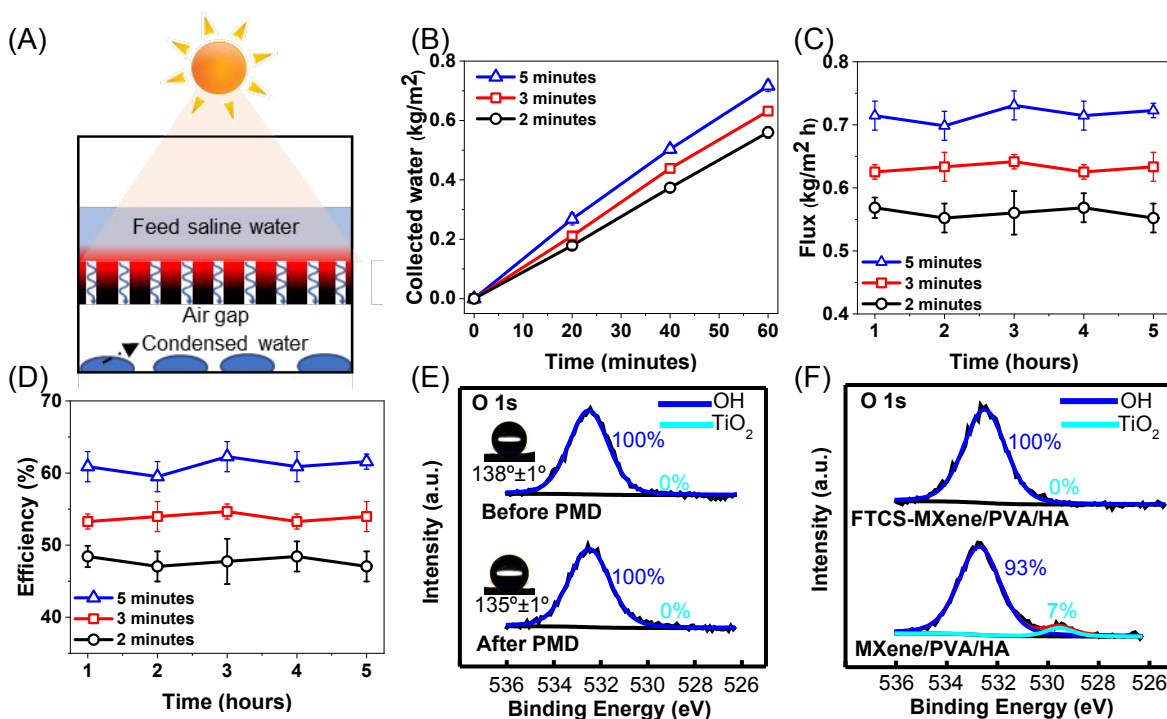
Figure 4. (A) Schematic illustration of AMD using FTCS-MXene/PVA/HA aerogel. (B) Collected water, (C) flux and (D) thermal efficiency of the PMD system using the FTCS-MXene/PVA/HA aerogel with varying feed water retention time, in purifying 0.5 M NaCl saline water under 0.8 sun irradiation over five consecutive cycles (each cycle for 1 hour, standard deviation obtained from measurements of 3 samples, error bars in (B) are smaller than the symbol size). (E) XPS of FTCS-MXene/PVA/HA aerogel before and after PMD test, insets show the contact angles of the aerogel before and after PMD test. (F) Comparison of XPS of FTCS-MXene/PVA/HA and MXene/PVA/HA aerogel after subjecting to 0.5 M NaCl solution for 1 week.

220

221   The thermal efficiencies (48%–61%) achieved on this MXene/PVA/HA aerogel is much

222   higher than the previously reported PMD thermal efficiency realized by PVDF-supported

223   photothermal membrane in treating ambient saline water, including carbon black nanoparticle-

224   coated PVDF membrane (~22%)[12] and polydopamine (PDA)-coated PVDF membrane (~45%)[68].

225   In addition, FTCS-MXene/PVA/HA aerogel is comparable to the highly efficient photothermal

226   membranes reported in PMD recently (Table S1). The superior PMD performance stems from the

227   high porosity of the composite aerogel. Because high porosity is critical for ensuring unimpeded

228   vapor transfer,[52] the higher porosity of MXene composite aerogel compared to previous PMD

229   membranes enables the same. Specifically, the porosity of carbon black nanoparticle-coated and

230   PDA-coated PVDF membrane was 65% and 75%, respectively, which are much lower than the

231   porosity of the MXene composite aerogel (91%). Apart from low vapor transfer resistance, this

232   MXene composite aerogel also exhibits optimal thermal management owing to its low thermal

233   conductivity, which makes its overall thermal efficiency comparable to the recently reported high-

234   performance bilayered photothermal membrane.[35, 43] Furthermore, incorporation of materials with

235   low thermal conductivity (*i.e.,* PVA and HA nanowires) suppresses the conductive heat transfer

236   during PMD, facilitating larger temperature difference across the aerogel and leading to a stronger

237   driving force for fast vapor transport.

238   **2.4 Stability of FTCS-MXene/PVA/HA composite aerogel**

239   FTCS-MXene/PVA/HA aerogel exhibited stable performance for over 5-cycles PMD test, and the

240   variations in the thermal efficiency were less than 2% (Figure 4D). To validate the long-term PMD

241   performance, the FTCS-MXene/PVA/HA aerogel was subjected to uninterrupted 12-hour PMD

242   test. The total amount of collected water for FTCS-MXene/PVA/HA aerogel was 4.5 g with water

243   retention time of 5 minutes, 3.9 g with water retention time of 3 minutes, and 3.3 g with water

244   retention time of 2 minutes, corresponding to a water flux of 0.73 $kg \cdot m^{-2} \cdot h^{-1}$, 0.63 $kg \cdot m^{-2} \cdot h^{-1}$ and

245   0.53 $kg \cdot m^{-2} \cdot h^{-1}$, respectively. The water flux under uninterrupted 12-hours of operation is similar

246   with that of cyclic test, suggesting the long-time stable performance. and the salt rejection was

247   around 99.98%. The Na^+ concentration of collected water was found to be within the range of

248   0.09 to 0.18 mM, which is far below the freshwater taste threshold defined by World Health

249   Organization (< 11 mM).[72]

250   Even after vigorous mechanical agitation to for 2 weeks, the FTCS-MXene/PVA/HA

251   aerogel did not display any signs of disintegration (Figure S5A), and no change in morphology

252   was observed (Figure S5B), highlighting the potential for long-term stability for PMD application.

253   We then evaluated the chemical stability of composite aerogel. The contact angle of FTCS-treated

254   MXene/PVA/HA was 138°±1° and 135°±1° before and after 5-cycles PMD test, respectively

255   (Figure 4E). The negligible change (variation less than 5%) in the contact angle of the aerogel

256   indicated the robust surface modification and durable hydrophobicity for stable desalination. The

257   chemical stability of MXene is important for long-term PMD performance. Based on previous

258   studies, MXene can be easily oxidized into TiO_2 in the presence of oxygen and water,[37, 73] resulting

259   in the deterioration in photothermal performance. While MXene-based solar evaporators have

260   been extensively investigated,[18, 19, 25, 74] chemical instability of MXene is still of significant concern

261   in their translation to real-world applications. Thus, the chemical composition of FTCS-treated

262   MXene before and after PMD performance was probed using XPS. The O 1s region revealed that

263   the peak attributed to TiO_2 at a binding energy of 529.9 eV[75] was virtually absent before and after

264   5-cycles PMD test, indicating the stable chemical structure of MXene over the multiple cycles

265   (Figure 5E). Considering the easy oxidation of $Ti_3C_2T_x$ in the presence of water and air, we posit

266   that the stability of $Ti_3C_2T_x$ stems from the FTCS treatment, which can prevent the direct

13

267   contacting of water with $Ti_3C_2T_x$. To validate this hypothesis, using O1s peak in XPS, we

268   monitored and compared the chemical composition of MXene/PVA/HA and FTCS-treated

269   MXene/PVA/HA aerogel after subjecting them to 0.5 M NaCl for 1 week (Figure 4F). For the

270   composite aerogel without FTCS, the oxygen peak associated with TiO_2 was discernable (with 7%

271   area under the peak attributed to TiO_2), whereas no discernable TiO_2-associate oxygen peak was

272   observed in the FTCS-treated aerogel. The excellent chemical stability of FTCS-treated

273   MXene/PVA/HA aerogel suggests that hydrophobic treatment is an effective method to prevent

274   the oxidation of $Ti_3C_2T_x$. Current approaches to avoid the oxidation of $Ti_3C_2T_x$ involves freeze

275   drying or the storage of $Ti_3C_2T_x$ colloids at low temperature (*e.g.*, aqueous solution at 4°C) in inert

276   atmospheres to slow down the oxidation process. However, these approaches are not applicable

277   for MXene-based solar evaporators. For the first time, our work first demonstrates the feasibility

278   of realizing MXene-based 3D architectures with high chemical stability for long-term stable solar-

279   driven desalination.

280   **2.5 Dual-mode antibiofouling capability**

281   To test the bactericidal ability, FTCS-treated MXene aerogel was exposed to *E. coli* in the culture

282   medium to induce the formation of biofilm (Figure 5A1). We have employed live/dead cell staining

283   assay to quantify the bactericidal activity of the aerogel. After 30-minutes growth without light

284   illumination, substantial green fluorescence was observed on the MXene composite aerogel

285   (Figure 5A2), suggesting the accumulation of live *E. coli* on the aerogel, and no signal of red

286   fluorescence was noted (Figure 5A3), indicating the absence of dead bacteria.
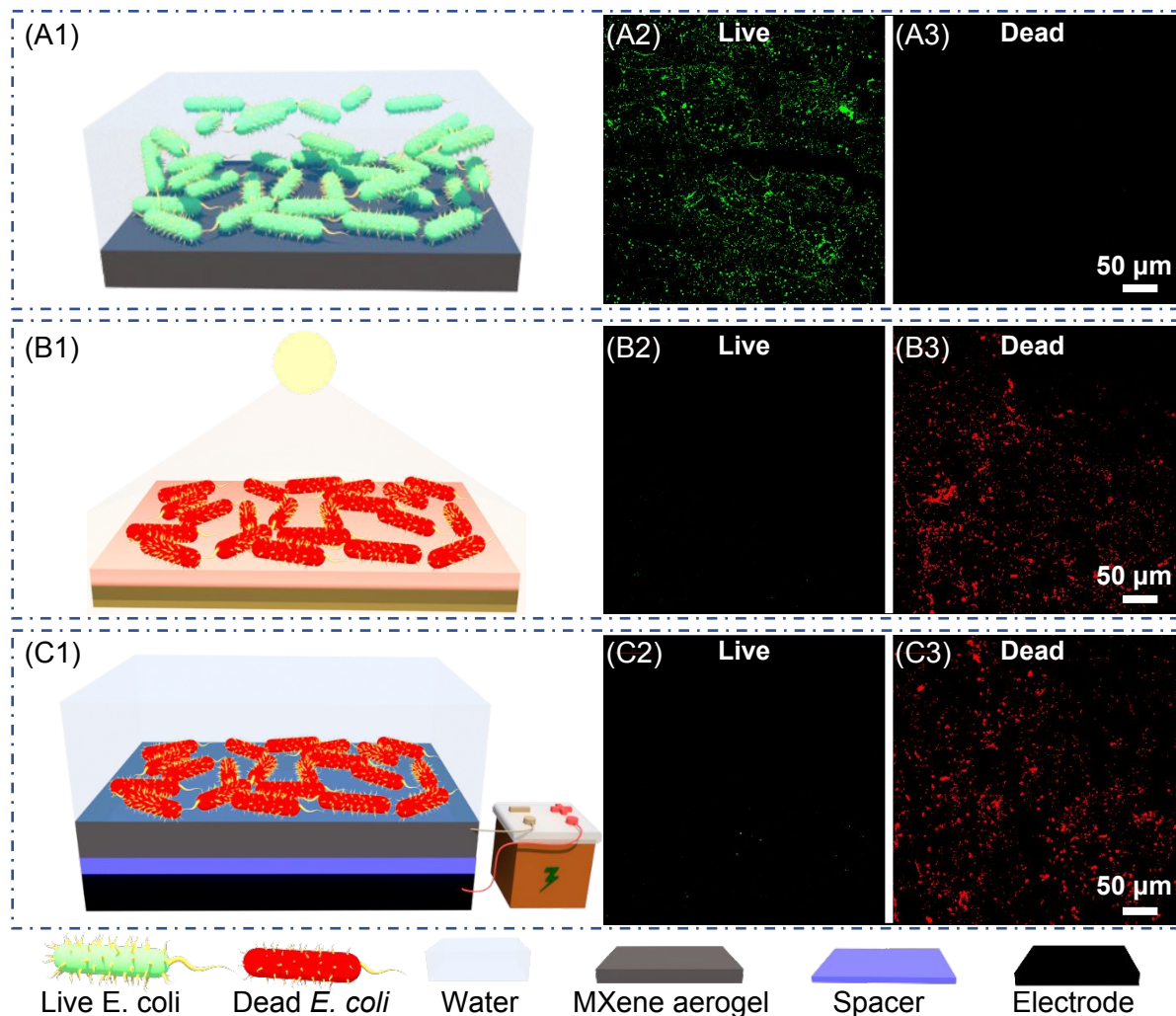
Live E. coli   Dead *E. coli*   Water   MXene aerogel   Spacer   Electrode

Figure 5. (A1) Schematic illustration showing the accumulation of *E. coli* on the surface FTCS-MXene/PVA/HA aerogel after exposure to the culture medium contaminated with *E. coli* for 30 minutes. Schematic illustration of antibiofouling performance enabled by FTCS-MXene/PVA/HA aerogel (B1) under solar irradiation in open air and (C1) after polarized with negative potential with a water thickness of 5 mm. Fluorescence images of *E. coli* on the surface of FTCS-MXene/PVA/HA aerogel (A2-A3) in pristine condition, (B2-B3) under solar irradiation in open air for 10 minutes and (C2-C3) after polarized with electric potential for 30 minutes.

287

288   To test the anti-biofouling performance, the *E. coli* adhered MXene composite aerogel was
289   either irradiated with solar light or subjected to electric potential. First, for testing photothermally
290   driven anti-biofouling, we drained the *E. coli* culture medium, and the composite aerogel was
291   irradiated with solar light with 0.8 sun (Figure 5B1). Only red fluorescence was observed, while
292   the green fluorescence disappeared, revealing that the solar irradiation was highly effective in
293   killing the bacteria. It is known that bacteria become inactivated at temperature above 55°C after
294   about five minutes.[76] Under sunlight irradiation, the surface temperature of MXene composite

295   aerogel reached up to 62 °C because of the photothermal effect, leading to effective disinfection

296   by local surface heating.

297   To test the electric field-induced anti-biofouling, the MXene composite aerogel was

298   integrated with a spacer and an electrode, as indicated in Figure 5C1. Then, negative voltage (-

299   3.0 V) was applied on the MXene composite aerogel covered with *E. coli* culture medium for 30

300   minutes to test the *in-situ* antibiofouling performance. Following the application of the voltage, we

301   noted that a relatively small fraction (< 1%) of the bacteria exhibited green fluorescence (Figure

302   5C2), indicating live bacteria, while most of the bacteria exhibited red fluorescence (Figure 5C3),

303   corresponding to the dead bacteria. These fluorescence images of MXene composite aerogel

304   indicate that bacteria can be effectively killed when the composite aerogel is subjected to electric

305   potential. MXene exhibits good conductivity,[77, 78] and the electrical conductivity of FTCS-treated

306   MXene composite aerogel was measured to be 7.8 µS/cm. Considering the charged surface can

307   damage the cell membrane structure directly,[44, 79] the MXene composite aerogel offers effective

308   disinfection after being polarized with external electric potential. This capability is particularly

309   important because sunlight can be intermittent. Moderate voltages required for effective

310   bactericidal activity can be easily achieved by solar powered batteries, avoiding the need for

311   additional energy sources. This electric field-induced antibiofouling performance serves as

312   alternative method for cost-effective disinfection when solar light is not adequate.

313   Next, we investigated the PMD performance FTCS-MXene/PVA/HA aerogel before

314   and after disinfection. After immersing in the *E. coli* solution for 30 minutes, the FTCS-

315   MXene/PVA/HA aerogel exhibited a water flux of 0.61 $kg·m^{-2}·h^{-1}$ with a water retention time

316   of 5 minutes under 0.8 sun irradiation for 30 minutes. Under identical test condition, the water

317   flux of FTCS-MXene/PVA/HA aerogel was 0.71 $kg·m^{-2}·h^{-1}$ and 0.70 $kg·m^{-2}·h^{-1}$ after

318   photothermal-driven disinfection and electric field-induced disinfection, respectively. The

319   water flux of FTCS-MXene/PVA/HA composite after disinfection was higher compared to

320   before disinfection, highlighting the importance of anti-biofouling property of MXene

321   composite aerogel in treating bacteria-contaminated water.

322   Therefore, based on excellent photothermal effect and electric conductivity, this MXene

323   composite aerogel shows versatile bactericide capability under solar irradiation or electric

324   potential. Compared with chemical treatment or physical cleaning, the built-in anti-biofouling

325   property of the MXene composite aerogel obviates the need for toxic chemicals or physical

326   processes damaging the membrane, making MXene aerogel highly appealing for treating

327   bacteria-contaminated water.

328   **3. Conclusion**

329   In summary, we have successfully designed and fabricated an efficient and anti-biofouling MXene

330   composite aerogel for highly efficient and stable PMD. The photothermal efficiency of the

331   MXene/PVA/HA aerogel reached 61% under 0.8 sun illumination. This performance is superior to

332   previously reported PVDF-supported photothermal membrane and comparable to recently

333   reported thermally-engineered photothermal membrane, in treating the saline water at room

334   temperature without any auxiliary heating system or heat recovery system. The as-prepared

335   MXene/PVA/HA aerogel exhibited excellent photothermal performance owing to the broadband

336   light absorption and high light-to-heat conversion efficiency of MXene. The high porosity and

337   interconnected porous network created by an ice-templating method resulted in a low resistance

338   to vapor transfer. Simultaneously, the composite aerogel exhibited low thermal conductivity,

339   significantly reducing the conductive heat transfer from the evaporative surface to the cold

340   permeate side and facilitating fast vapor transfer. FTCS-treatment minimized oxidation of MXene,

341   providing excellent chemical stability to MXene/PVA/HA aerogel even under prolonged exposure

342   to saline water. Furthermore, due to the inherent photothermal properties and electrical

343   conductivity, MXene composite aerogel exhibited bactericidal activity under both solar irradiation

344   and external electric potential. Owing to high thermal efficiency, chemical stability and versatile

345   bactericidal activity, MXene composite aerogel is highly attractive in treating ambient saline water

346   by utilizing the abundant sunlight, which is highly appealing for the freshwater generation in the

347   remote regions and disaster-struck communities.

348   **4. Experiments**

349   **4.1 Synthesis of $Ti_3C_2T_x$ MXene flakes**

350    $Ti_3C_2T_x$ MXene flakes were synthesized by selectively etching the Al layer of Ti_3AlC_2 using LiF/HCl

351   as previously reported.[16] Specifically, LiF (2 g, Alfa Aesar) was added to the HCl (9M, 40 ml,

352   Millipore Sigma) solution under stirring in a Teflon vessel to obtain homogeneous solution. Then,

353   Ti_3AlC_2 powder (1 g, Shanghai Chenyue Metal Co., Ltd, China) was slowly added to the LiF/HCl

354   solution, and the mixture was transferred to an oil bath at 35 °C and left under stirring for 24 hours.

355   The resultant suspension was centrifuged at 3500 rpm for 5 minutes. After decanting the

356   supernatant, the collected product was dispersed in water. This wash step was repeated until the

357   pH of suspension was ~6. Finally, the suspension was subjected to sonication for 1 hour to

358   delaminate the multilayer $Ti_3C_2T_x$ under Ar flow. After centrifuging at 3500 rpm for 1 hour, the

359    $Ti_3C_2T_x$ flakes colloid was obtained by collecting the supernatant. After bubbling Ar for 20 minutes,

360   the collected $Ti_3C_2T_x$ colloid was stored at 4 °C in a sealed vial.

361   **4.2 Fabrication of MXene/PVA/HA aerogel and PVA/HA aerogel**

362   HA nanowires were synthesized by the calcium oleate precursor *via* solvothermal reaction

363   reported previously.[35] After dispersing the PVA powder (Mw 8,000~10,000, Millipore Sigma) in

364   water, the mixture was kept in an oil bath at 60 °C for 2 hours under stirring to obtain a

365   homogeneous solution. PVA solution (50 mg/ml, 0.5 ml) was added to $Ti_3C_2T_x$ colloid (17 mg/ml,

366   0.5 ml). Then, HA nanowires suspension (5 mg/ml, 1 ml) was added the homogenous mixture of

367    $Ti_3C_2T_x$ and PVA. To fabricate PVA/HA aerogel, HA nanowires suspension (1 ml), the PVA

368   solution (0.5 ml) and water (0.5 ml) were mixed homogeneously. To fabricate aerogel, the mixture

369   was transferred to a petri dish with a diameter of 5.5 cm. After complete freezing at -20 °C, the

370   mixture was freeze dried for 24 hours at -80 °C to obtain the aerogel.

371   **4.3 Hydrophobic treatment**

372   To convert the hydrophilic aerogel to hydrophobic aerogel, the MXene/PVA/HA aerogel was

373   treated with (tridecafluoro-1,1,2,2-tetrahydrooctyl) trichlorosilane (FTCS, Millipore Sigma) vapor

374   in a sealed container at 70 °C for 24 hours. Water contact angle of the aerogel was measured

375   using a contact angle analyzer (Phoenix 300, Surface Electro Optics Co. Ltd) to confirm the

376   hydrophobicity after FTCS treatment.

377   **4.4 Optical properties and photothermal performance**

378   Reflectance and transmittance spectra of aerogels were measured using a CRAIC micro

379   spectrophotometer (QDI 302) coupled to a Leica optical microscope (DM 4000M) with a 20×

380   objective in the range of 450–800 nm with 10 accumulations and 100 milliseconds exposure time

381   in reflection and transmission mode, respectively. The surface temperature of aerogel with a size

382   of 1 cm × 1 cm was monitored using an IR camera (FLIR E8-XT) under light illumination using a

383   solar simulator (Newport 66921 Arc Lamp) with light intensity of 0.8 kW•m^{-2}, as measured by a

384   spectroradiometer (SpectriLight ILT 950).

385   **4.5 Thermal conductivity measurement**

386   The thermal conductivities of the MXene/PVA/HA aerogel were measured by monitoring the

387   temperature distribution across the thickness of aerogel that were sandwiched between two glass

388   microscope slides. The bottom glass slide was in contact with a hot plate and the top glass slide

389   was in contact with ice. The temperature of the hot plate was increased from 70 °C to 120 °C, in

390 steps of 10 °C. The vertical temperature distribution for the sandwich was monitored using a high-

391 speed IR camera (Telops FAST M3k). The emissivity coefficient of a glass slide and a sample

392 was assumed to be 0.9 to obtain the temperature distribution.[80] The Fourier equation was used

393 to calculate the thermal conductivity of the aerogel:

394
$$q' = K\frac{\Delta T}{\Delta X}$$

395   The heat flux (q') was calculated by assuming the thermal conductivity (K) of 1.05

396 $W{\cdot}m^{-1}{\cdot}K^{-1}$ for glass slides. Because the glass slide and samples experience the same heat flux,

397 the heat flux value obtained for the glass slide was used to measure the thermal conductivity of

398 the MXene/PVA/HA aerogel.

4.6 Nano- and micro-structure characterization

400 Scanning electron microscope (SEM) images of the surface and the cross-section of the aerogel

401 and the nanowires were obtained after sputter coating the samples with gold. A FEI Nova 2300

402 field-emission SEM was used at an acceleration voltage of 10.5 kV. Atomic force microscopy

403 (AFM) image was obtained using Dimension 3000 (Bruker) in light tapping mode. V-shaped silicon

404 cantilever (Micromash) with a nominal tip radius of 8 nm were used for the imaging. The porosity

405 was measured using isopropanol *via* previous reported solvent replacement method.[43]

4.7 Chemical stability measurement

407 X-ray photoelectron spectroscopy (XPS, PHI 5000 VersaProbe II, Ulvac-PHI with monochromatic

408 Al Kα radiation) was utilized to measure the O 1s spectra of MXene to understand chemical nature

409 and changes in the chemical functionality of MXene. The contact angle and XPS of FTCS-treated

410 MXene/PVA/HA aerogel was monitored after 5-cycles PMD test. To investigate the effect of

411 hydrophobic treatment on the long-term stability, pristine MXene/PVA/HA aerogel and FTCS-

412 treated MXene/PVA/HA aerogel were immersed in 0.5 M NaCl solution for 1 week, respectively,

413 and their chemical functionality was monitored and compared using XPS.

4.8 Photothermally-driven membrane distillation performance measurement

415 The PMD performance was evaluated using an air gap membrane distillation (AMD) module. The

416 PMD cell was constructed using acrylonitrile butadiene styrene (ABS) plastic by 3D printing. The

417 diameter of the MD cell was 3 cm, while the diameter of the membrane surface that was exposed

418 to sunlight was measured to be 2.8 cm. The light illumination to AMD was achieved using a solar

419 simulator under 0.8 sun illumination. NaCl aqueous solution (0.5 M) was employed as the feed

420 water. The ambient feed water was continuously pumped using a peristaltic pump (model WPX1-

421　　F1/8S4−C, Welco Co. Ltd., Tokyo), with a flow rate of 1.57 ml•min^{-1}, 1.06 ml•min^{-1} and 0.62

422　　ml•min^{-1} to achieve water retention time of 2 minutes, 3 minutes and 5 minutes, respectively. The

423　　thickness of the feed water was maintained at 5 mm. Aluminum foil was used as the condensation

424　　surface on the permeate side with a 2 mm air gap. The amount of collected water was recorded

425　　using a weight scale (Sartorius ELT402).

426　　　　　The thermal efficiency of the photothermal membrane was determined by the ratio of heat

427　　flux required to generate distillate flux to the total irradiated solar flux, $\eta = \frac{mh_{vap}}{I}$, where $\dot{m}$

428　　represents the distillate flux of water, h_{vap} refers to the total evaporation enthalpy change, and I is

429　　the total incident solar flux. Given the water evaporation enthalpy of 2454 kJ•kg^{-1} (~0.68

430　　kW•kg^{-1}•h^{-1}), the thermal efficiency was calculated based on the input solar flux and distillate flux.

431　　**4.9 Antibiofouling test**

432　　To test the bactericidal activity, the *E. coli* (pC013, Addgene) were cultured in Luria-Bertani (LB)

433　　liquid broth at 37 °C. All cultures were in 500 ml sterilized shake flasks (100 ml working volume,

434　　shaking at 250 rpm). After 12-hours culture, *E. coli* (~6.4x10^8 live cells/ml) were harvested. A layer

435　　of *E. coli* biofilm was formed on the surface of FTCS-treated MXene/PVA/HA aerogel by exposing

436　　it to the feed solution comprised of LB medium with *E. coli* for 30 minutes. To test the photothermal

437　　disinfection ability, the feed solution was removed from the aerogel and followed by 10-minutes

438　　sunlight irradiation with a light intensity of 0.8 kW•m^{-2}. To evaluate the bactericidal activity under

439　　electric potential, a two-electrode system consisting of a compact MXene film (~ 4 μm) and a

440　　polypropylene membrane as a spacer (3501 Coated PP, Celgard LLC) was employed. MXene

441　　film was fabricated by vacuum filtration of MXene colloids. The conductivity of MXene composite

442　　aerogel was measured using a four-point conductivity cell (BT-110, Scribner Associates).

443　　Negative potential (- 3.0 V) was applied on the aerogel for 30 minutes. The electrical potential

444　　was applied with a DC power supplier (Dr. Meter DC Power Supply HY3005D). The biofilm on the

445　　composite aerogel was monitored using fluorescent dyes (Molecular Probes Live/Dead Bacterial

446　　cell viability kit, Thermo Fisher Scientific), and the fluorescence images were collected using

447　　confocal laser scanning microscope (20× objective, Zeiss LSM 880 Laser Scanning Confocal

448　　Microscope) to identify the live bacteria and dead bacteria.

449　　**4.10 Mechanical agitation**

450　　Owing to the difficulty in conducting mechanical test on the thin aerogel (*e.g.* compression

451　　test), the FTCS-MXene/PVA/HA aerogel was subjected to mechanical agitation to

452　　validate its mechanical stability. The aerogel (1 cm × 1 cm, *L* × *W*) was placed in a 50 mL

453   test tube filled with water, then it was subjected to rigorous mechanical agitation in a tube

454   rotator (VWR Multimix Tube Rotator Mixer 13916-822) for 2 weeks.

455   **Conflicts of interest**

456   There are no conflicts to declare.

457   **Acknowledgements**

References

1. Y.-S. Jun, X. Wu, D. Ghim, Q. Jiang, S. Cao and S. Singamaneni, *Accounts of Chemical Research*, 2019, **52**, 1215-1225.
2. A. Alkhudhiri, N. Darwish and N. Hilal, *Desalination*, 2012, **287**, 2-18.
3. C. Chen, Y. Kuang and L. Hu, *Joule*, 2019, **3**, 683-718.
4. S. Cao, P. Rathi, X. Wu, D. Ghim, Y.-S. Jun and S. Singamaneni, *Advanced Materials*, **n/a**, 2000922.
5. D. Ghim, Q. Jiang, S. Cao, S. Singamaneni and Y.-S. Jun, *Nano Energy*, 2018, **53**, 949-957.
6. Y. Kuang, C. Chen, S. He, E. M. Hitz, Y. Wang, W. Gan, R. Mi and L. Hu, *Advanced Materials*, 2019, **31**, 1900498.
7. S. Cao, Q. Jiang, X. Wu, D. Ghim, H. Gholami Derami, P.-I. Chou, Y.-S. Jun and S. Singamaneni, *Journal of Materials Chemistry A*, 2019, **7**, 24092-24123.
8. G. Ni, S. H. Zandavi, S. M. Javid, S. V. Boriskina, T. A. Cooper and G. Chen, *Energy & Environmental Science*, 2018, **11**, 1510-1519.
9. L. Zhu, M. Gao, C. K. N. Peh, X. Wang and G. W. Ho, *Advanced Energy Materials*, 2018, **8**, 1702149.
10. Y.-S. Jun, D. Ghim, X. Wu, S. Cao and S. Singamaneni, *HDIAC Journal*, 2019, **6**, 6.
11. A. Politano, P. Argurio, G. Di Profio, V. Sanna, A. Cupolillo, S. Chakraborty, H. A. Arafat and E. Curcio, *Advanced Materials*, 2017, **29**, 1603504.
12. P. D. Dongare, A. Alabastri, S. Pedersen, K. R. Zodrow, N. J. Hogan, O. Neumann, J. Wu, T. Wang, A. Deshmukh, M. Elimelech, Q. Li, P. Nordlander and N. J. Halas, *Proceedings of the National Academy of Sciences of the United States of America*, 2017, **114**, 6936-6941.
13. H. Gholami Derami, Q. Jiang, D. Ghim, S. Cao, Y. J. Chandar, J. J. Morrissey, Y.-S. Jun and S. Singamaneni, *ACS Applied Nano Materials*, 2019, **2**, 1092-1101.
14. B. Anasori, M. R. Lukatskaya and Y. Gogotsi, *Nature Reviews Materials*, 2017, **2**, 16098.
15. S. Hong, F. Ming, Y. Shi, R. Li, I. S. Kim, C. Y. Tang, H. N. Alshareef and P. Wang, *ACS Nano*, 2019, **13**, 8917-8925.
16. M. Alhabeb, K. Maleski, B. Anasori, P. Lelyukh, L. Clark, S. Sin and Y. Gogotsi, *Chemistry of Materials*, 2017, **29**, 7633-7644.
17. Z. Xie, Y. Duo, Z. Lin, T. Fan, C. Xing, L. Yu, R. Wang, M. Qiu, Y. Zhang, Y. Zhao, X. Yan and H. Zhang, *Advanced Science*, 2020, **7**, 1902236.
18. R. Li, L. Zhang, L. Shi and P. Wang, *ACS Nano*, 2017, **11**, 3752-3759.
19. Q. Zhang, G. Yi, Z. Fu, H. Yu, S. Chen and X. Quan, *ACS Nano*, 2019, **13**, 13196-13207.
20. J. H. Kim, G. S. Park, Y.-J. Kim, E. Choi, J. Kang, O. Kwon, S. J. Kim, J. H. Cho and D. W. Kim, *ACS Nano*, 2021, **15**, 8860-8869.
21. X. Ming, A. Guo, Q. Zhang, Z. Guo, F. Yu, B. Hou, Y. Wang, K. P. Homewood and X. Wang, *Carbon*, 2020, **167**, 285-295.
22. J. Liu, H.-B. Zhang, X. Xie, R. Yang, Z. Liu, Y. Liu and Z.-Z. Yu, *Small*, 2018, **14**, 1802479.
23. M. C. Krecker, D. Bukharina, C. B. Hatter, Y. Gogotsi and V. V. Tsukruk, *Advanced Functional Materials*, 2020, **30**, 2004554.
24. D.-D. Shao, Q. Zhang, L. Wang, Z.-Y. Wang, Y.-X. Jing, X.-L. Cao, F. Zhang and S.-P. Sun, *Journal of Membrane Science*, 2021, **623**, 119033.
25. L. Tang, X. Zhao, C. Feng, L. Bai, J. Yang, R. Bao, Z. Liu, M. Yang and W. Yang, *Solar Energy Materials and Solar Cells*, 2019, **203**, 110174.
26. J. Zhao, Y. Yang, C. Yang, Y. Tian, Y. Han, J. Liu, X. Yin and W. Que, *Journal of Materials Chemistry A*, 2018, **6**, 16196-16204.
27. J. Liu, H.-B. Zhang, R. Sun, Y. Liu, Z. Liu, A. Zhou and Z.-Z. Yu, *Advanced Materials*, 2017, **29**, 1702367.

28. X. Zhao, X.-J. Zha, L.-S. Tang, J.-H. Pu, K. Ke, R.-Y. Bao, Z.-y. Liu, M.-B. Yang and W. Yang, *Nano Research*, 2020, **13**, 255-264.
29. X. Fan, Y. Yang, X. Shi, Y. Liu, H. Li, J. Liang and Y. Chen, *Advanced Functional Materials*, **n/a**, 2007110.
30. X. Zhao, L.-M. Peng, C.-Y. Tang, J.-H. Pu, X.-J. Zha, K. Ke, R.-Y. Bao, M.-B. Yang and W. Yang, *Materials Horizons*, 2020, **7**, 855-865.
31. K. Li, T.-H. Chang, Z. Li, H. Yang, F. Fu, T. Li, J. S. Ho and P.-Y. Chen, *Advanced Energy Materials*, 2019, **9**, 1901687.
32. Y. Z. Tan, H. Wang, L. Han, M. B. Tanis-Kanbur, M. V. Pranav and J. W. Chew, *Journal of Membrane Science*, 2018, **565**, 254-265.
33. L. Chen, X. Shi, N. Yu, X. Zhang, X. Du and J. Lin, *Materials*, 2018, **11**, 1701.
34. H. Gholivand, S. Fuladi, Z. Hemmat, A. Salehi-Khojin and F. Khalili-Araghi, *Journal of Applied Physics*, 2019, **126**, 065101.
35. S. Cao, X. Wu, Y. Zhu, R. Gupta, A. Tan, Z. Wang, Y.-S. Jun and S. Singamaneni, *Journal of Materials Chemistry A*, 2020, **8**, 5147-5156.
36. Y. Lee, S. J. Kim, Y.-J. Kim, Y. Lim, Y. Chae, B.-J. Lee, Y.-T. Kim, H. Han, Y. Gogotsi and C. W. Ahn, *Journal of Materials Chemistry A*, 2020, **8**, 573-581.
37. Y. Chae, S. J. Kim, S.-Y. Cho, J. Choi, K. Maleski, B.-J. Lee, H.-T. Jung, Y. Gogotsi, Y. Lee and C. W. Ahn, *Nanoscale*, 2019, **11**, 8387-8393.
38. C. J. Zhang, S. Pinilla, N. McEvoy, C. P. Cullen, B. Anasori, E. Long, S.-H. Park, A. Seral-Ascaso, A. Shmeliov, D. Krishnan, C. Morant, X. Liu, G. S. Duesberg, Y. Gogotsi and V. Nicolosi, *Chemistry of Materials*, 2017, **29**, 4848-4856.
39. F. Xia, J. Lao, R. Yu, X. Sang, J. Luo, Y. Li and J. Wu, *Nanoscale*, 2019, **11**, 23330-23337.
40. Q. Jiang, D. Ghim, S. Cao, S. Tadepalli, K.-K. Liu, H. Kwon, J. Luan, Y. Min, Y.-S. Jun and S. Singamaneni, *Environmental Science & Technology*, 2019, **53**, 412-421.
41. I. Luzinov, S. Minko and V. V. Tsukruk, *Progress in Polymer Science*, 2004, **29**, 635-698.
42. M. C. Vasudev, K. D. Anderson, T. J. Bunning, V. V. Tsukruk and R. R. Naik, *ACS Applied Materials & Interfaces*, 2013, **5**, 3983-3994.
43. X. Wu, S. Cao, D. Ghim, Q. Jiang, S. Singamaneni and Y.-S. Jun, *Nano Energy*, 2021, **79**, 105353.
44. L. Jiang, L. Chen and L. Zhu, *Water Research*, 2019, **161**, 297-307.
45. Y. Baek, H. Yoon, S. Shim, J. Choi and J. Yoon, *Environmental Science & Technology Letters*, 2014, **1**, 179-184.
46. C.-F. de Lannoy, D. Jassby, K. Gloe, A. D. Gordon and M. R. Wiesner, *Environmental Science & Technology*, 2013, **47**, 2760-2768.
47. X.-J. Zha, X. Zhao, J.-H. Pu, L.-S. Tang, K. Ke, R.-Y. Bao, L. Bai, Z.-Y. Liu, M.-B. Yang and W. Yang, *ACS Applied Materials & Interfaces*, 2019, **11**, 36589-36597.
48. D.-D. Qin, Y.-J. Zhu, F.-F. Chen, R.-L. Yang and Z.-C. Xiong, *Carbon*, 2019, **150**, 233-243.
49. Z.-C. Xiong, Y.-J. Zhu, D.-D. Qin, F.-F. Chen and R.-L. Yang, *Small*, 2018, **14**, 1803387.
50. G. Liu, J. Shen, Q. Liu, G. Liu, J. Xiong, J. Yang and W. Jin, *Journal of Membrane Science*, 2018, **548**, 548-558.
51. M.-Q. Zhao, X. Xie, C. E. Ren, T. Makaryan, B. Anasori, G. Wang and Y. Gogotsi, *Advanced Materials*, 2017, **29**, 1702410.
52. D. Hou, T. Li, X. Chen, S. He, J. Dai, S. A. Mofid, D. Hou, A. Iddya, D. Jassby, R. Yang, L. Hu and Z. J. Ren, *Science Advances*, 2019, **5**, eaaw3203.
53. P. Wang, *Environmental Science: Nano*, 2018, **5**, 1078-1089.
54. M. Fujiwara, *Desalination*, 2017, **404**, 79-86.
55. M. Fujiwara and M. Kikuchi, *Water Res.*, 2017, **127**, 96-103.
56. P. D. Dongare, A. Alabastri, S. Pedersen, K. R. Zodrow, N. J. Hogan, O. Neumann, J. Wu, T. Wang, A. Deshmukh and M. Elimelech, *Proc. Natl. Acad. Sci.*, 2017, **114**, 6936-6941.

57. X. Wu, Q. Jiang, D. Ghim, S. Singamaneni and Y.-S. Jun, *J. Mater. Chem. A*, 2018, **6**, 18799-18807.

58. L. Huang, J. Pei, H. Jiang and X. Hu, *Desalination*, 2018, **442**, 1-7.

59. Y. Z. Tan, H. Wang, L. Han, M. B. Tanis-Kanbur, M. V. Pranav and J. W. Chew, *J. Membr. Sci.*, 2018, **565**, 254-265.

60. Y. Tian, M. Zhou, H. Shi, S. Gao, G. Xie, M. Zhu, M. Wu, J. Chen and Z. Niu, *Nano Letters*, 2018.

61. B. Gong, H. Yang, S. Wu, J. Yan, K. Cen, Z. Bo and K. K. Ostrikov, *ACS Sustainable Chem. Eng.*, 2019, **7**, 20151-20158.

62. B. Gong, H. Yang, S. Wu, G. Xiong, J. Yan, K. Cen, Z. Bo and K. Ostrikov, *Nano-Micro Lett.*, 2019, **11**, 51.

63. X. Han, W. Wang, K. Zuo, L. Chen, L. Yuan, J. Liang, Q. Li, P. M. Ajayan, Y. Zhao and J. Lou, *Nano Energy*, 2019, **60**, 567-575.

64. S. Cao, X. Wu, Y. Zhu, R. Gupta, A. Tan, Z. Wang, Y.-S. Jun and S. Singamaneni, *J. Mater. Chem. A*, 2020, **8**, 5147-5156.

65. J. Huang, Y. Hu, Y. Bai, Y. He and J. Zhu, *Desalination*, 2020, **489**, 114529.

66. W. Li, Y. Chen, L. Yao, X. Ren, Y. Li and L. Deng, *Desalination*, 2020, **478**, 114288.

67. Y. Zhang, K. Li, L. Liu, K. Wang, J. Xiang, D. Hou and J. Wang, *Chemosphere*, 2020, 127053.

68. X. Wu, Q. Jiang, D. Ghim, S. Singamaneni and Y.-S. Jun, *Journal of Materials Chemistry A*, 2018, **6**, 18799-18807.

69. X. Wu, S. Cao, D. Ghim, Q. Jiang, S. Singamaneni and Y.-S. Jun, *Nano Energy*, 2020, 105353.

70. Y. Peng, Y. Wang, W. Li and J. Jin, *Journal of Materials Chemistry A*, 2021, **9**, 10678-10684.

71. M. Gryta, *Journal of Membrane Science*, 2008, **325**, 383-394.

72. P. Zhang, Q. Liao, H. Yao, Y. Huang, H. Cheng and L. Qu, *Energy Storage Materials*, 2019, **18**, 429-446.

73. T. Habib, X. Zhao, S. A. Shah, Y. Chen, W. Sun, H. An, J. L. Lutkenhaus, M. Radovic and M. J. Green, *npj 2D Materials and Applications*, 2019, **3**, 8.

74. X. Zhao, X.-J. Zha, J.-H. Pu, L. Bai, R.-Y. Bao, Z.-Y. Liu, M.-B. Yang and W. Yang, *Journal of Materials Chemistry A*, 2019, **7**, 10446-10455.

75. J. Halim, K. M. Cook, M. Naguib, P. Eklund, Y. Gogotsi, J. Rosen and M. W. Barsoum, *Applied Surface Science*, 2016, **362**, 406-417.

76. A. T. Spinks, R. H. Dunstan, T. Harrison, P. Coombes and G. Kuczera, *Water Research*, 2006, **40**, 1326-1332.

77. Z. Wu, T. Shang, Y. Deng, Y. Tao and Q.-H. Yang, *Advanced Science*, 2020, **7**, 1903077.

78. Z. Wang, S. Kang, S. Cao, M. Krecker, V. V. Tsukruk and S. Singamaneni, *MRS Bulletin*, 2020, **45**, 1017-1026.

79. V. R. Krishnamurthi, A. Rogers, J. Peifer, I. Niyonshuti, J. Chen and Y. Wang, *bioRxiv*, 2020, 2020.2003.2013.991067.

80. Q. Jiang, L. Tian, K.-K. Liu, S. Tadepalli, R. Raliya, P. Biswas, R. R. Naik and S. Singamaneni, *Advanced Materials*, 2016, **28**, 9400-9407.